Eng. Sci., 2023, **24**, 899

Engineered Science
DOI: https://dx.doi.org/10.30919/es899

# An Electro-Mechanical Coupled Model For 3D Printed Piezoelectrets: Development, Validation, And Prediction

Xiaolin Wang,[1, 2] Zhe Liu,[1, 2] Hui Wang[1, 2] and Changchun Zeng[1, 2,*]

## Abstract

Piezoelectric polymer foams (Piezoelectrets) are space-charged porous materials with a wide range of applications. Mathematical models have been developed to understand the influences of the porous structure on the piezoelectric properties. These models omit the details of the pore structures and their effects on the mechanical and electrical characteristics, limiting the capability to qualitative prediction only. In this paper, an electro-mechanical coupled model was established for quantitative prediction of the piezoelectric properties of 3D printed piezoelectrets. The model takes into consideration of the pore structures details and their deformation, the accompanied charge development, and their coupled effects. To validate the model, a series of piezoelectrets with pre-defined structure parameters were designed and 3D printed using fused filament fabrication (FFF). Their piezoelectric properties were characterized. The model calculated piezoelectric coefficient $d_{33}$ of piezoelectrets were in excellent agreement with the experimentally measured values. We finally demonstrated the excellent quantitative predictive capability of the model by using an out-of-sample set of piezoelectrets. The developed model can be used to guide the design of piezoelectrets structures for desired piezoelectric performance.

*Keywords:* Piezoelectret; Piezoelectric coefficient; Modeling; Fused deposition modeling.
Received: 07 February 2023; Revised: 22 May 2023; Accepted: 22 May 2023.
Article type: Research article.

## 1. Introduction

Piezoelectrets are space charged porous polymers[1-4] with high piezoelectricity. The charge variation of the piezoelectrets results from the deformation of the charged pores and change of the electrical dipole under external pressure. Because of the ease of deformation of the porous polymer structures comparing to solid polymers or ceramics, piezoelectrets can achieve significantly higher piezoelectric sensitivity than piezoelectric ceramics such as lead zirconate titanate (PZT)[5-7] or piezoelectric polymers such as polyvinylidene fluoride (PVDF).[8,9] A great deal of research has been explored in fabricating piezoelectrets using a wide variety of polymer materials including polypropylene (PP),[10-13] cyclic olefin copolymer (COC),[14-16] fluorinated ethylene propylene (FEP)[17-19] and polyethylene naphthalate (PEN).[20] Devices including piezoelectric sensors,[21,22] actuators[23,24] and energy harvesters[25,26] were reported previously. Among all the polymers, PP remains the most commonly used piezoelectrets due to their high flexibility, amenable mass processability and low cost. Compared to piezoelectric ceramic or polymers, the piezoelectrets are highly deformable, customizable, and designable. They can be designed and tailored to fit the specific demands.

The piezoelectric sensitivity of piezoelectrets is typically characterized by the direct piezoelectric coefficient $d_{33}$, which is expressed by Eq. (1):[27]

$$d_{33} = \frac{\Delta Q}{\Delta F} = k\frac{\sigma}{Y} \tag{1}$$

where Q is the charge variation, F is the applied force, Y is the Young's modulus and σ is the electric charge densities. k is related to the material dielectric properties. The Young's modulus for the porous polymer materials can be expressed as Eq. (2);[28]

$$Y_p = Y_s\phi^2/A \tag{2}$$

where $Y_p$ is the Young's modulus of the polymer foam, $Y_s$ is the Young's modulus of the solid polymer material, Φ is the porosity and A is the pore aspect ratio. The structure parameters of a unit cell were illustrated in Fig. 1.

As shown in Fig. 1, the pore aspect ratio is calculated by Eq. (3):

$$A = \frac{d}{h} \tag{3}$$

---

[1] *Department of Industrial and Manufacturing, FAMU-FSU College of Engineering, Tallahassee, FL 32310, USA.*
[2] *High-Performance Materials Institute, Florida State University, Tallahassee, FL 32310, USA*
*Email:* zeng@eng.famu.fsu.edu (C. Zeng)

Therefore, to obtain high piezoelectric performance, piezoelectrets with large porosity and large pore aspect ratio is in need.

To render piezoelectricity, the porous structure is subjected to electrical charging. The charge density σ is related to the charging voltage according to the following Eq. (4):[2]

$$\sigma = C(V - V_{bd}) \tag{4}$$

where C is a constant related to the dielectric properties of the polymer, V is the applied charging voltage, $V_{bd}$ is the characteristic onset voltage of dielectric breakdown of the gas in the porous structure. $V_{bd}$ follows the Paschen's law (discussed later in detail) and is a function of the pillar height h.

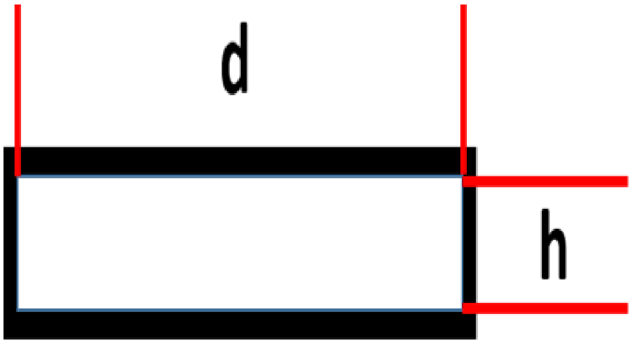

**Fig. 1** Illustration of the unit cell in the piezoelectrets.

Therefore, both modulus and the electric charge densities are determined by the geometry of the pore structures of the piezoelectrets, and the piezoelectric performance ($d_{33}$) of the piezoelectrets is related to the porous structure in a complicated manner. Understanding the structure-electromechanical properties by modeling would greatly facilitate the structure-piezoelectric property relationship and achieve tailored piezoelectric performance by rational geometry design of the pore structure. Previously a multi-layer model[29] was proposed; however, this model was unable to quantitatively predict the performance of the piezoelectrets. This may be the results of the simplification and assumptions made in the model that neglects several key physical aspects. First, the model assumes the porous structure to be an alternating layer of polymer-gas. Therefore, the effect of the pore structure, e.g., aspect ratio and boundary conditions, are ignored. Secondly, the deformation of the porous structures is considered to be homogeneous in this model. However, the deformation of the real pore structure is much more complicated and most likely not uniform. And the deformation behavior would significantly affect the piezoelectric performance of the piezoelectrets.

Therefore, an electrical-mechanical coupled model considering both the porous structure geometry and charging effect is in highly desired to direct the fabrication of the piezoelectrets. At the same time, a manufacturing method with excellent structural controllability would not only aid the model validation but also used for the piezoelectret fabrication with model predicted performance.

In recent years 3D printing has emerged as a highly accurate, highly customizable and low cost[30-32] to realize structures with controlled geometry. In our previous work we demonstrated the feasibility of using fused filament fabrication (FFF) to 3D print PP electrets.[33] In this paper, 3D printing (FFF) was employed to print a series of PP piezoelectrets with designed structure parameters. Separately, an electrical-mechanical coupled model incorporating the pore geometry and deformation details, and their influence of charging, were developed. In this model, beam theory was employed to study the mechanical deformation of the piezoelectrets whereas Paschen's law and Gauss' law were employed to predict the surface charge density and the charge density development from the mechanical deformation. To validate the model, the piezoelectric coefficient $d_{33}$ of the 3D printed piezoelectrets were measure and compared with the model calculation. The predictive capability was further verified. Piezoelectrets with new structure parameters were fabricated under the guidance of the model and the predicted $d_{33}$ values agreed very well with the measured values. The models have great potential in guiding the design of the piezoelectrets.

## 2. Materials and methods

### 2.1Piezoelectrets fabrication

### 2.1.1 3D printing of porous structures

The basic porous structure printed in the study is a 5-layer non-overlap structure following our previous study.[33] The overall structure and the mechanical deformation of the prototype under external pressure was illustrated in Figs. 2(a) and (b). The structure parameters including the solid layer thickness $h_1$, pillar height $h_2$, pillar space d and pillar width w were illustrated in Fig. 2(c). Such structure possess low moduli and was highly deformable under pressure.[14,16]

In this study the solid polymer height $h_1$ is fixed to 0.1 mm and the pillar width w is fixed to 0.2 mm. They were chosen to ensure successful printing of the overhang structure with sufficient structure integrity and fidelity based on the previous feasibility study.[33] The design flexibility was realized by varying pillar height $h_2$, pillar space d, which allow for tuning of the porosity, deformation behavior and charging characteristics. The detailed design of the structure parameters is shown in Table 1.

**Table 1.** Structure parameters for the designed structures.

| d(mm)<br>$h_2$(mm) | 3 | 4 | 5 | 6 |
|---|---|---|---|---|
| 0.3 | P1-1 | P2-1 | P3-1 | P4-1 |
| 0.4 | P1-2 | P2-2 | P3-2 | P4-2 |
| 0.5 | P1-3 | P2-3 | P3-3 | P4-3 |
| 0.6 | P1-4 | P2-4 | P3-4 | P4-4 |

Fused filament fabrication (FFF) was used for the fabrication process. It has been proven that FFF is feasible in fabricating the piezoelectrets.[33] Polypropylene (PP) filament

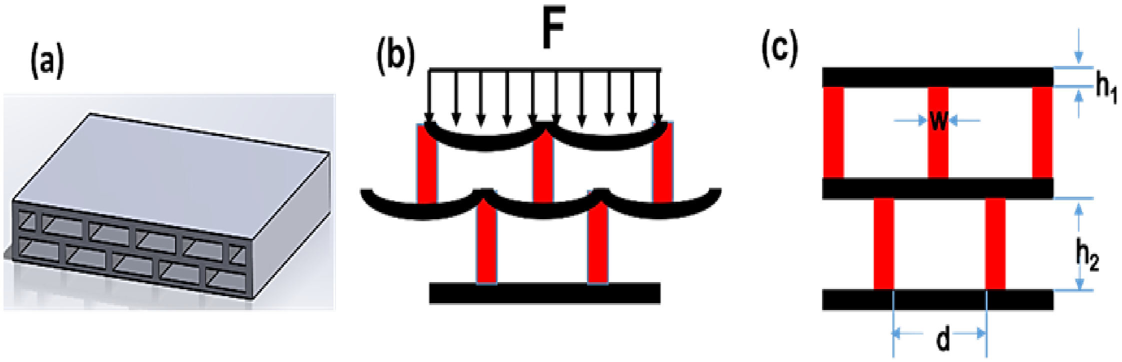

**Fig. 2** Illustration of the non-overlap structure (a); Illustration of the deformation of the non-overlap structure under pressure(b); and unit cell to show the structure parameters and (c).

used for printing was purchased from Gimzo Dorks. Lulzbot TAZ5 purchased from Lulzbot was used for 3D printing of the porous structure. The nozzle diameter was 0.2 mm and the controlling software was cura-lulzbot edition. Other printing parameters were the following: printing temperature 210 ℃, speed 10 mm/s, flow rate 120%. Each single printing layer height is 0.1 mm.

### 2.1.2 Charging of the as-printed porous structure

A 1×1 $cm^2$ square copper electrode was placed on both the top and bottom layer of the 3D printed piezoelectrets. In this paper, the conductive copper tape was directed attached to the sample surface. Aerosol jet or inkjet printing might be employed in the future[34-36] to create better conductive circuit. Then the samples were charged by contact charging using a precision high voltage power supply (PNC10000-6ump, Heinzinger electronic Gmnh) at room temperature. The voltage employed was 8 kV and the charging process lasts for 12 s. Finally, the charged samples were placed in aluminum foil for 24 h for the stabilization of the accumulated charges before the piezoelectric characterization.

## 2.2 Piezoelectrets characterization

### 2.2.1 Characterization of the printing quality and structure fidelity

Optical images taken by dino camera was employed to characterize the morphology of the samples. Both the top view and the side view of the samples were characterized to show both the overall morphology and the overhang structure quality. Top view images were first taken for the as-printed samples in a 20x magnification to show the printing quality and the overall structures. Then the samples were cut by laser to a 5×1 $cm^2$ rectangular shape for the side view image. A 50x magnification was selected to show the morphology and dimensions of the unit cell for the detailed structure information. The measured structure parameters in the optical images were employed to compare with the designed values to show the overall printing qualities.

### 2.2.2 Charge build-up characterization

Hysteresis loop measurements were performed to study the electrical properties of the piezoelectrets. All the tests were performed using Precision Premier II (Radiant technologies, Inc.) in bi-polar mode (TREK Model 609B) with the charging voltages varied from 1kv to 9kv. The voltage interval selected is 500V. The hysteresis loop of each voltage was then conducted, and the remnant polarization strength $P_r$ was recorded. For each voltage, averaged $P_r$ from 5 tests were employed for further calculation.

### 2.2.3 Piezoelectric property characterization

Quasi-static piezoelectric coefficient $d_{33}$ were measured in a Faraday cage using the well-known equation: $d_{33}=Q/F$, in which Q is the induced charge and F is the applied force. A pre-load of 0.2N was applied on the top surface of the sample to minimize the possible air gap effect in all measurements. A set of pre-calibrated loads F varies from 0.1N to 2N were applied onto the sample to a 1×1 $cm^2$ square electrode, then quickly removed. The induced charge Q were recorded and integrated in 10s by a Keithley electrometer (6517A, Keithley Instruments, Inc.). Values averaged from 5 separate measurements for each sample were calculated and recorded.

## 3. Development of electromechanical coupled model

### 3.1 General considerations

As we have demonstrated in the introduction part, the $d_{33}$ can be calculated by Eq. (1). Both of the electrical charge density and the young's modulus were determined by the structure parameters d and h. Therefore, the key point in establishing the electromechanical model is to fully investigate the impacts of the structural parameters on the electrical charge density and the mechanical displacement. To date, the most commonly used model is the multi-layer model with alternating polymer/air layer structures. The structure is shown in Fig. 3(a). The model omits the details on the pore geometry and the boundary limitations of the unit cells, therefore is not capable of guiding the design of the porous structure. In this paper, we developed an improved model in two steps. The two steps are shown in Figs. 3(a) and (b). In the first step, we use the multi-layer model to study the correlation between the surface charge densities and the pillar height $h_2$ and to investigate the general charge density variation over the

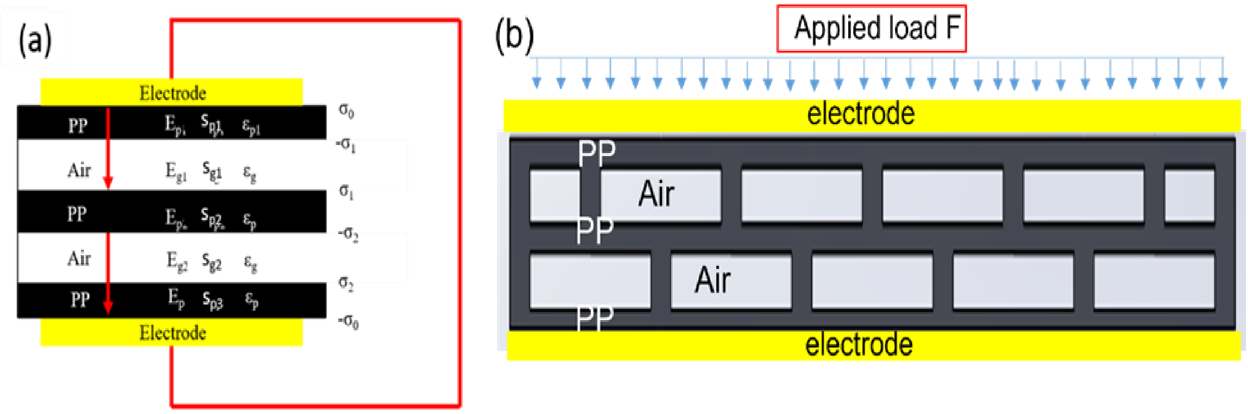

**Fig. 3** Illustration of the model build process. (a) Electrical model and (b) mechanical model.

change of the pillar height induced by the external forces. In the second step, we studied the deformation behavior of a unit cell under external pressure with the pore geometry considered. Then we calculate the charge density variation at each position by employing the charge density-pillar height correlation obtained from the electric model and the overall charge density variations are integrated over a unit cell. The $d_{33}$ is then calculated from Eq. (1).

### 3.2 Charge density modeling

The basic electrical model was shown in Fig. 3(a). There are two goals in building the electric model: (1) study the correlation between the surface charge density and the pillar height $h_2$; and (2) study how the charge density varies with the change of the pillar height $h_2$.

The charge build-up process was illustrated in Fig. 4. Piezoelectret charging is a two-step process. During the first stage, the electrical potential on the external surfaces of the piezoelectrets increase linearly as the charging voltage increases. However, there is no charge accumulation at the internal polymer/gas interface. Once the charging voltage is removed, the surface potential falls back to 0. The process does not result in any permanent charges and the materials are not piezoelectric. When the voltage further increases to over a characteristic voltage (Stage II), i.e., the Paschen breakdown voltage, dielectric breakdown[29,37] takes places resulting in charges begin to accumulate in the polymer/gas interfaces. The materials become piezoelectric at this stage, and the piezoelectricity increases with the increase of the charging voltage. The increase of the charge density over the applied voltage follows Eq. (5):

$$\sigma_i = C(V_{gi} - V_{bd}) \tag{5}$$

where $\sigma_i$ is the charge density, C is a constant determined by the electric properties of the polymer materials. $V_{gi}$ is the distributed voltage in the air layer, $V_{bd}$ is the breakdown voltage. Both are determined by the pore geometry and can be expressed as Eqs. (6) and (7):

$$V_{gi} = \frac{\varepsilon s_{gi}}{s_p + \varepsilon s_g} V_{total} \tag{6}$$

$$V_{bd} = \frac{B p s_g}{ln(A p s_g) - ln[\, ln(1 + \frac{1}{\gamma_{se}})]} \tag{7}$$

where ε is the relative dielectric constant of the polymer (2.1). $V_{total}$ is the charging voltage, $s_{gi}$ is the thickness of the $i^{th}$ air layer; $s_p$ and $s_g$ is the total thickness of the air layer and polymer layer.

A is the saturation ionization in gas, B is related to the excitation and ionization energies, p is the pressure in pascals, and $\gamma_{se}$ is the secondary-electron-emission coefficient. For air with an E/p in the range of 450 to 7500 V/(kpa • cm), A, B and $\gamma_{se}$ can be considered as constant with the values 112.5 (cm • kpa)$^{-1}$, 2737.5 V/(cm • kpa), and 0.1, respectively.[38]

Next step is to study the impacts of the pillar height variation on the change of the charge densities. As shown in Fig. 3(a), for the uppermost polymer/air interface, in the short circuit condition, Gauss's law can be expressed as Eq. (8):

$$-\varepsilon_0 \varepsilon_p E_{p1} + \varepsilon_0 E_{g1} = -\sigma_1 \tag{8}$$

where $E_{p1}$ is the electric strength in the uppermost polymer layer and $E_{g1}$ is the electric strength in the uppermost air layer. $\sigma_1$ is the charge density in the first polymer/air interface. Similar relation holds for other PP/air interface.

The Kirchhoff's second law in the short circuit condition for the overall piezoelectrets can be written as Eq. (9):

$$\sum_i s_{pi} E_{pi} + \sum_i s_{gi} E_{gi} = 0 \tag{9}$$

$E_{p1}=E_{p2}=E_{p3}=E_1$ can be obtained from those equations and furthermore, The $E_1$ and $E_{gi}$ can be written as Eqs. (10) and (11):

$$E_1 = -[\varepsilon_0(s_1 + \varepsilon s_2)]^{-1} \sum_i s_{gi} \sigma_i \tag{10}$$

$$E_{gi} = \frac{\sigma_1}{\varepsilon_0} - [\varepsilon_0(s_1 + \varepsilon s_2)]^{-1} \varepsilon \sum_i s_{gi} \sigma_i \tag{11}$$

where $E_{gi}$ is the electric strength in the i-th air layer, $\sigma_i$ is the charge density in i-th polymer/air interface.

For the top surface, the Gauss law can be written as and Eq. (12):

$$\sigma_0 = -\varepsilon_0 \varepsilon E_1 \tag{12}$$

Based on Eqs. (10) and (12), the correlation between the surface charge density and the polymer/air interface charge density can be expressed as Eq. (13):

$$\sigma_0 = \varepsilon[(s_1 + \varepsilon s_2)]^{-1} \sum_i s_{gi} \sigma_i \tag{13}$$

The surface charge density $\sigma_0$ was correlated with the structure parameter $s_1$, $s_{gi}$ and the charge density in the polymer/air interface $\sigma_i$ in this electric model.

In the multilayer structures with fixed structural parameters, the thickness of each individual air layer height $s_{gi}$ is the same. Based on Eqs. (5)-(7), the polymer/air interface electric charge density $\sigma_i$ is the same. Thus, the $\sigma_i$ can be simplified to $\sigma_1$ and the correlation between $\sigma_1$ and $\sigma_0$ can be expressed as Eq. (14):

$$\sigma_1 = -\frac{(s_1\varepsilon_g + s_2\varepsilon)\sigma_0}{\varepsilon s_2} \tag{14}$$

In the short-circuit condition, the change of the charge on the top electrode is mainly resulted from the change of the thickness of the air layers.

Moreover, $\frac{\partial\sigma_i}{\partial s_2} = \frac{s_{2i}}{s_2}$ and $\frac{\partial\sigma_0}{\sigma_0} = \frac{\partial s_2}{s_2}$ can be assumed based on the following considerations: i) the electric charge density results from the macro-level dipole moments which are formed by the porous structure (bubble geometry and dimension). Therefore, the charge density is directly correlated with the thickness of the piezoelectrets; ii) 2) due to the negligibly low young's modulus of the air compared with the bulk polypropylene (PP), the deformation of the overall sample can be viewed as the deformation of the air layer only. Thus the thickness of the polymer layer remains the same in the deformation. The charge density is then correlated to the air layer thickness $s_2$; iii) the charge density is determined by the Paschen's law. In the experiment values we used in this paper (1atm, 0.3-0.6 mm), it can be viewed as linearly change. Then $\frac{\partial\sigma_0}{\partial s_2}$ followed Eq. (15):

$$\frac{\partial\sigma_0}{\partial s_2} = \frac{\varepsilon\sum_i s_{2i}\sigma_i}{s_2(s_1+\varepsilon s_2)} \tag{15}$$

The charge density variation induced by the variation of the pillar height can be calculated by Eq. (15).

### 3.3 Mechanical deformation modelling

The deformation of the non-overlap structure was modeled in this section using the unit cell illustrated in Fig. 3(b). Only a half cell is used because of the structure symmetry. For polymer layer with large aspect ratio (A>10), the deformation of the polymer/air interface is similar to that of a beam which is already well-studied in the solid mechanics. A repeating unit of the porous structure was shown in Fig. 5(c). For the top layer, the deformation can be viewed as a beam under a uniformed distributed force. The deformation at position x can be calculated by the beam theory with two fixed ends.[39] The deformation can be calculated by Eq. (16).

$$H_1(x) = \frac{Fd^3}{24EI}\left(\frac{x^4}{d^4} - 2\frac{x^3}{d^3} + \frac{x^2}{d^2}\right) \tag{16}$$

Where F is the applied force, E (1300Mpa) is the elastic modulus for the solid polymer layer, d is the pillar space, and I is the inert momentum which can be calculated by Eq. (17):

$$I = \frac{bh^3}{12} \tag{17}$$

Where h (0.1 mm) is the thickness of the solid layer and b (20 mm) is the width of the sample.

For the third layer, the deformation resulted from the beam under the force applied at the center point. The deformation at position x can be written as Eq. (18):

$$H_2(x) = \frac{Pd^3}{48EI} - \frac{Pd^3}{12EI}\left(\frac{3({}^{d}/_{2}-x)}{4d} - \frac{({}^{d}/_{2}-x)^3}{d^3}\right) \tag{18}$$

Where P is the transferred load induced by the applied force F.

Therefore, the deformation of the first air layer is calculated by Eq. (19):

$$\Delta s_{21} = H_1(x) + H_2(x) \tag{19}$$

The deformation of the second air layer is shown in Eq. (20):

$$\Delta s_{22} = \frac{Pd^3}{12EI}\left(\frac{3(\frac{d}{2}-x)}{4d} - \frac{(\frac{d}{2}-x)^3}{d^3}\right) \tag{20}$$

The total deformation at the position x can be calculated by Eq. (21).

$$\Delta s_2 = \Delta s_{21} + \Delta s_{22} \tag{21}$$

### 3.4 Electrical-mechanical coupled model.

In a unit cell, at position x, the differential total deformation is calculated by Eq. (22):

$$ds_2 = ds_{21} + ds_{22} = \left[\frac{Fd^3}{24EI}\left(\frac{x^4}{d^4} - 2\frac{x^3}{d^3} + \frac{x^2}{d^2}\right) + \frac{Pd^3}{192EI}\right] \tag{22}$$

And the resulting change of the top surface charge $d\sigma_0$ was shown in Eq. (23), which based on Eq. (15)

$$d\sigma_0 = \varepsilon\frac{\sum_i s_{2i}\sigma_i}{s_2(s_1+\varepsilon s_2)}ds_2 \tag{23}$$

The charge variation in the half unit cell can be written as Eq. (24):

$$\Delta\sigma_0 = \int_0^{\frac{L}{2}} d\sigma_0 dx =$$

$$\int_0^{\frac{L}{2}} \varepsilon\frac{\sum_i s_{2i}\sigma_i}{s_2(s_1+\varepsilon s_2)}\left[\frac{Fd^3}{24EI}\left(\frac{x^4}{d^4} - 2\frac{x^3}{d^3} + \frac{x^2}{d^2}\right) + \frac{Pd^3}{192EI}\right]dx \tag{24}$$

The electrical charge density at each layer $\sigma_i$ is the same and can be written as $\sigma_1$.

This leads to Eq. (25):

$$\Delta\sigma_0 = 2\int_0^{\frac{L}{2}} d\sigma_0 dx =$$

$$2\int_0^{\frac{L}{2}} \varepsilon\frac{\sigma_1}{(s_1+\varepsilon s_2)}\left[\frac{Fd^3}{24EI}\left(\frac{x^4}{d^4} - 2\frac{x^3}{d^3} + \frac{x^2}{d^2}\right) + \frac{Pd^3}{192EI}\right]dx \tag{25}$$

Integration of the above yields Eq. (26):

$$\Delta\sigma_0 = 2\varepsilon\left[\frac{d^4P}{384EI(\varepsilon s_2+s_1)} + \frac{d^4F}{1440EI(\varepsilon s_2+s_1)}\right]\sigma_1 \tag{26}$$

Based on Eqs. (14) and (26), the induced charge variation $\Delta Q$ in a unit cell can be expressed as Eq. (27):

$$\Delta Q = b\Delta\sigma_0 = 2\left[\frac{d^4P}{384EI} + \frac{d^4F}{1440EI}\right]\frac{b}{s_2}\sigma_0 \tag{27}$$

where b is the sample width, and it is fixed to 20 mm for all samples. This is the induced charge under applied force F. For a unit cell, F=P as shown in Fig. 5(b). Therefore $d_{33}$ is written as Eq. (28):

$$d_{33} = \frac{\Delta Q}{F} = \frac{2\left[\frac{d^4P}{384EI} + \frac{d^4F}{1440EI}\right]\frac{b}{s_2}\sigma_0}{F} = \left[\frac{d^4}{384EI} + \frac{d^4}{1440EI}\right]\frac{b\sigma_0}{s_2} = \frac{19bd^4\sigma_0}{2880\varepsilon EIs_2} = \frac{19d^4\sigma_0}{240\varepsilon Eh^3s_2} \tag{28}$$

In the Eq. (28), $s_2$, h and d are the structural parameters, E is the elastic modulus of the polypropylene, ε is the dielectric constant of the PP and $\sigma_0$ is the surface charge density. Due to

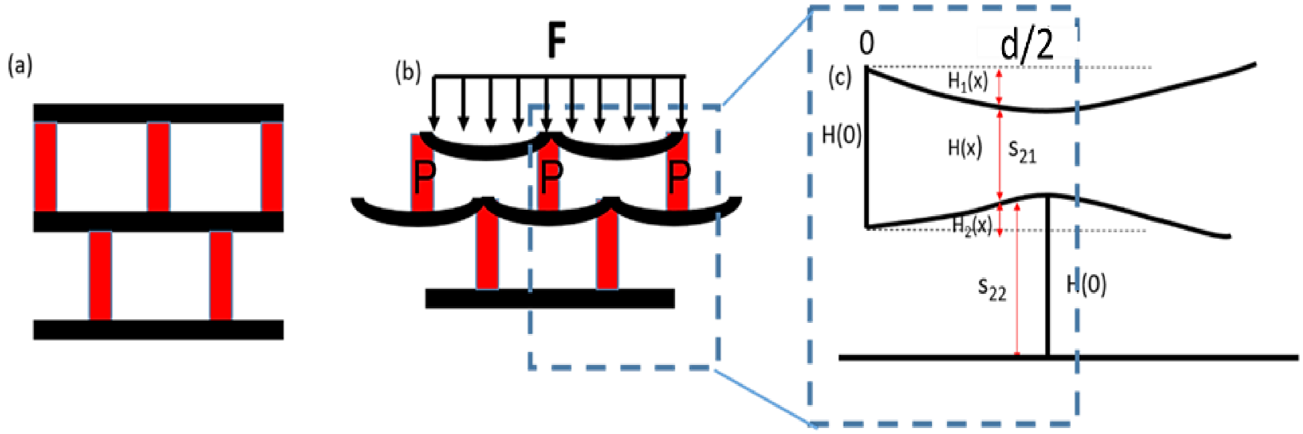

**Fig. 5** illustration of the non-overlap structure without pressure (a) or under pressure (b), deformation in a unit cell (c).

the extreme complex electro-physical interactions at the polymer/air interfaces, the surface charge density $\sigma_0$ is difficult to be calculated analytically and needs to be experimentally determined. Once this input is obtained, the piezoelectric coefficient can be predicted using only the pore geometric parameters and basic material mechanical and dielectric properties.

## 4. Results and discussion

### 4.1 Morphology of the 3D printed piezoelectrets

Piezoelectrets with designed geometries were 3D printed and used for model validation and prediction. To achieve this, it is critical that the printed structures conform to the design in terms of the geometric accuracy. In addition, high surface quality (without cracks or defects on the printed solid layers) is essential to ensure charge storage capability.[33]

Using the printing parameters discussed in the experimental section, the series of porous structures (Table 1) were successfully printed and used for subsequent charging and piezoelectric characterization. A representative example of the printed piezoelectret is shown in Fig. 6. Fig. 6(a) shows a photograph of the printed sample. Fig. 6(b) shows the top surface and Fig. 6(c). is a cross-section view of sample.

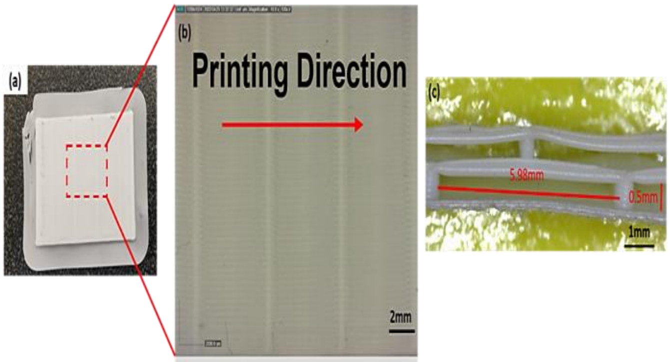

**Fig. 6** Morphology of the 3D-printed piezoelectric polymer foams. The overall structures, surface quality and the overhang structure accuracy were shown in (a), (b) and (c), respectively.

As shown in Fig. 6(b), there are no obvious defects or cracks in the top surface layer of the printed sample. The printed overhang structure is shown in Fig. 6(c). Both the pillar space and pillar height in the printed sample was essentially the same as the design (designed pillar height = 0.5 mm, pillar space 6 mm). Sagging of the printed solid layer was acceptable even with the largest pillar space and was expected to be less severe in all other printed samples. Overall, the printed samples conformed well to the design. They were used for model validation.

### 4.2 Partial model validation of the electric model

Previous research has shown the hysteresis loop of the piezoelectrets are only determined by the pillar height $h_2$ and the solid layer height $h_1$.[34] Thus, samples P1-1 to P1-4 with the pillar height $h_2$ varied from 0.3mm to 0.6 mm were selected to validate the electric model. The hysteresis loops for samples P1-1 to P1-4 were shown in Fig. 7. Typical ferroelectric curves were shown, and the remnant polarization strengths were recorded. With the increase of the charging voltage, both the maximum polarization strength $P_{max}$ and the remnant polarization strength $P_r$ increases. The charge density of the piezoelectrets is determined by the only the remnant polarization strength $P_r$, not the $P_{max}$. Thus, the detailed correlations between $P_r$ with the charging voltage were summarized in Fig. 7(e). At a particular voltage (breakdown voltage), the $P_r$ begins to accumulate and shows a near-linear dependency of the charging voltage. The breakdown voltages for the sample P1-1, P1-2, P1-3 and P1-4 are approximate 4.5kv, 5kv, 5.5kv and 6.5kv, respectively. It increases with the increase of the pillar height.

As a partial model validation, the theoretical breakdown voltages for these porous structures were calculated using Paschen's law (Eq. 7) and compared with the measure values. Table 2 summarizes the results.

The calculated results are in reasonable agreement with the measured values in general, which shows the designed structures could be well realized, and that the charging process indeed is a dielectric breakdown process. The slightly higher calculated values may be the result of slight sagging of the overhang structure, which would lead to reduction of the pillar height.

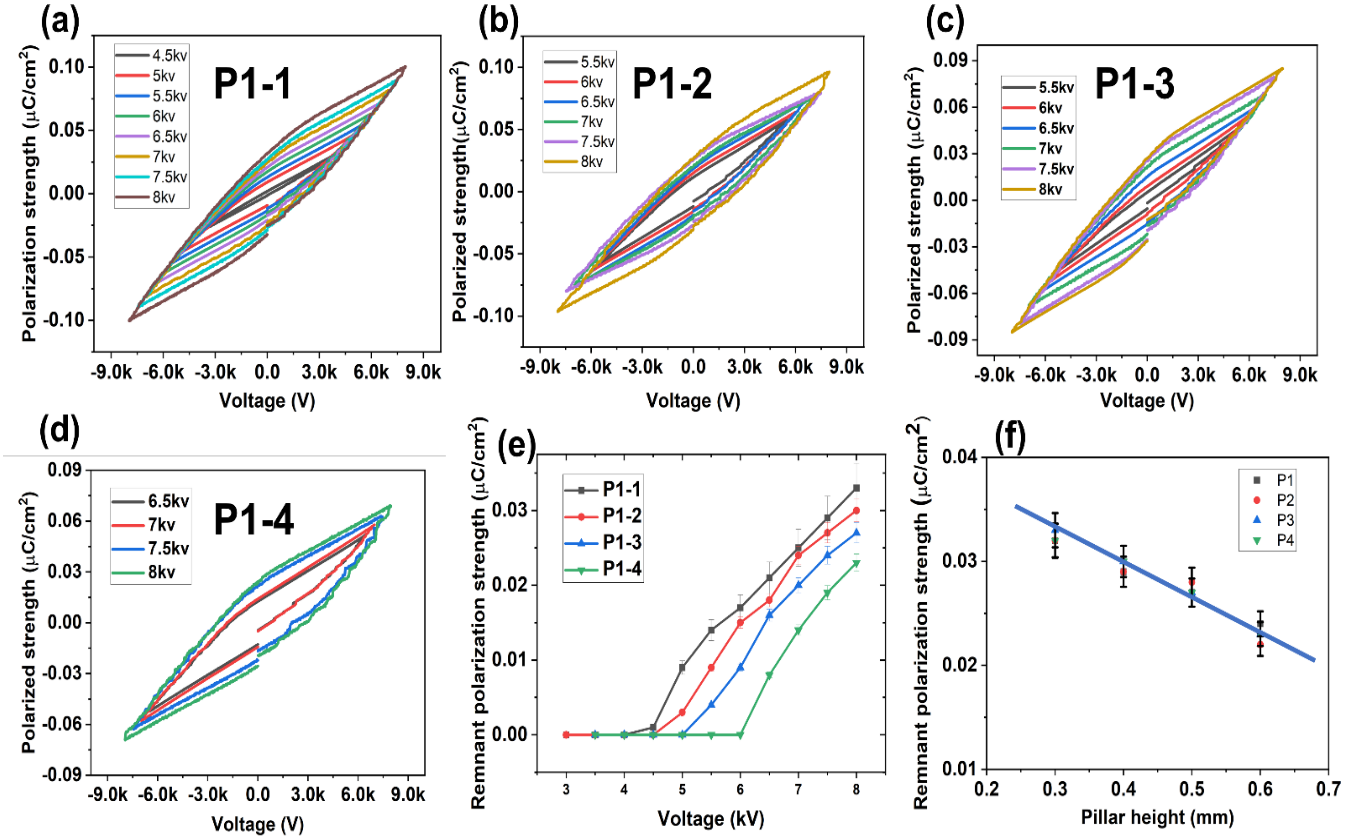

**Fig. 7** Hysteresis loop for piezoelectrets with different pillar height (a) to (d), the pillar height is 0.3 mm (a), 0.4 mm (b), 0.5 mm (c) and 0.6 mm (d), respectively. The remnant polarization strength under different charging voltage is shown in (e) and the correlation between the pillar space and the remnant polarization strength is shown in (f).

**Table 2.** Summary of the measured values and calculated values of the breakdown voltage of the piezoelectrets with different pillar height.

| Pillar height(mm) | Measured $V_{bd}$ | Calculated $V_{bd}$ |
|---|---|---|
| 0.3 | 4500 | 4684 |
| 0.4 | 5000 | 5620 |
| 0.5 | 5500 | 6274 |
| 0.6 | 6500 | 7053 |

The correlation between the $P_r$ with the pillar height $h_2$ was shown in Figs. 7(e) and (f). A clear linearity can be observed for all the samples as predicted by Eq. (4). With the increase of $h_2$ from 0.3 mm to 0.6 mm, the remnant polarization strength decreases linearly from 0.033μC/cm² to 0.023μC/cm². The measured charge density values were employed for further model calculations.

### 3.3 Validation and prediction of the electric-mechanical coupled model.

Sample P1 to P3 were selected to validate the electric-mechanical coupling model. The measured piezoelectric coefficients ($d_{33}$) and the model calculated $d_{33}$ values of the samples from P1 to P3 were shown in Fig. 8(a). The impact of the pillar space d and the pillar height h were illustrated in Fig. 8(a) as well. First, it is obviously that the $d_{33}$ increased with the increase of the pillar space d. From sample P1-1 to P3-1, with a pillar height fixed to 0.3 mm, the $d_{33}$ values varied from 120 pC/N to 1100 pC/N as the pillar space increased from 3 mm to 5 mm. Secondly, the $d_{33}$ decreases with the increase of the pillar height. From the sample P3-1 to P3-4, with the pillar space fixed to 5 mm, $d_{33}$ decreased from 1100 pC/N to around 400 pC/N with the pillar height changed from 0.3 to 0.6 mm. The comparison between the measured values and the model predicted values are shown in Fig. 8(b). As shown in Fig. 8(b), the model calculated matched very well with the experimental measurements.

In the following part, the electro-mechanical coupled model was employed to predict the $d_{33}$ with new structure parameters. A total number of 4 out-of-sample data was collected for prediction of the model. The 4 samples are P4-1, P4-2, P4-3, and P4-4 with a fixed 6 mm pillar space while the pillar height varied from 0.3 to 0.6 mm. Three tests were performed for each sample and the average $d_{33}$ values were recorded. The experiment values and model predicted values were shown in Fig. 9. The model can predict the $d_{33}$ with high degree of accuracy comparing to the experimental values. It should also be noted that the 3d printed piezoelectrets achieved a maximum $d_{33}$ of 2300 pC/N, comparable to the best performing piezoelectrets reported in the literature.

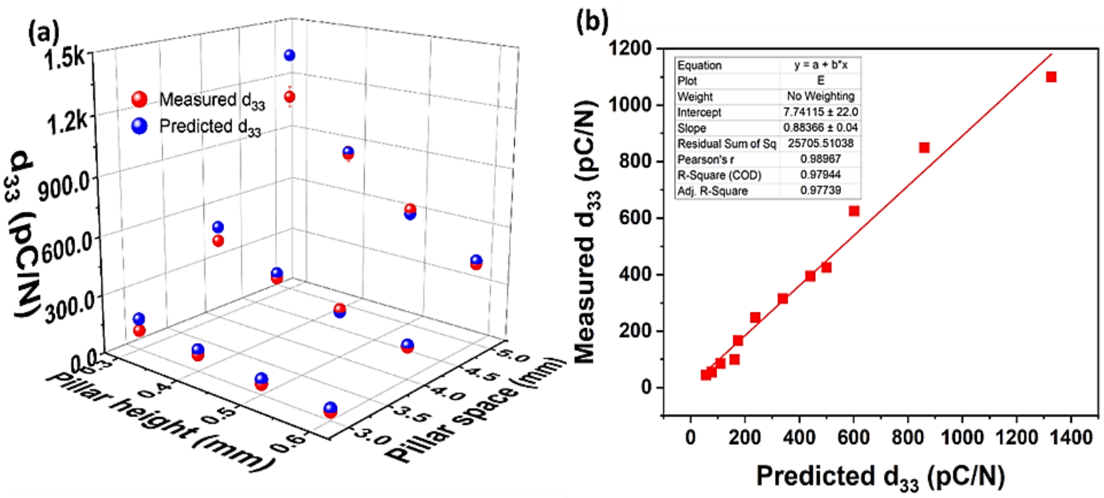

**Fig. 8** Validation of the electrical-mechanical coupled model. (a) Measured $d_{33}$ values (red dots) and model predicted $d_{33}$ values (blue dots) of the piezoelectrets with samples P1 to P3; (b) comparison and correlation of the measured $d_{33}$ values to the model predicted values.

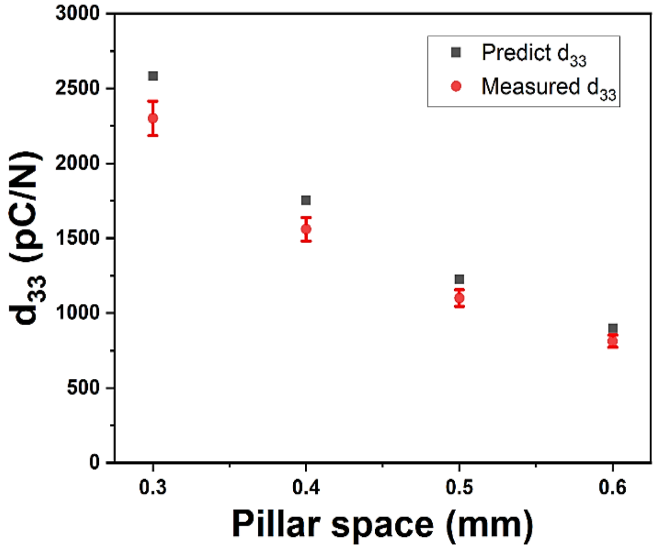

**Fig. 9** Model predicted $d_{33}$ values vs. measured $d_{33}$ values for sample P4-1to P4-4.

In summary, the developed model was fully validated and is capable to predict the structure-piezoelectric coefficient relationship. It can be used to direct the 3D printing of piezoelectrets with targeted performance. The current limitation in the electro-mechanical coupling model is the boundary conditions induced by the pillar width is not considered, which may resulted to the small discrepancies between the measured $d_{33}$ values and the model predicted $d_{33}$ values. This problem needs to be resolved in the future. Furthermore, Similar methodology could be employed in more porous structures other than the non-overlap structures to further improve the overall performance of the piezoelectrets. It is also important to note that the developed model may not be accurate for piezoelectrets under large deformation because the mechanical model was based on small deformation.

## 5. Conclusion

In this study we developed an electro-mechanical coupled model to quantitatively predict the structure-piezoelectric coefficient relationship of piezoelectrets with a non-overlap structure. The charging process and induced surface charge development under mechanical deformation were modeled by application Paschen's law, Gauss' law, and Kirchhoff's second law. Beam theory was adopted to model the deformation behavior of the non-overlap structure. Combination of the two aspects yielded a mechanism-based model that captured the essential structural, mechanical, and electromechanical attributes of the piezoelectrets. The model was validated by comparing the predicted performance of piezoelectrets to that of 3D printed piezoelectrets with the same structure parameters. Moreover, the model was capable of accurately predicting the piezoelectric coefficient $d_{33}$ for piezoelectrets with provided structural parameters. This predictive capability, along with the 3D printing technology we developed to realize with high fidelity the designed structure, provides a versatile and effective tool to fabricate piezoelectrets with designed structure and piezoelectric activity that are optimized for the intended applications such as piezoelectric sensors. Compared with traditional thin film sensors, the 3D-printed structural sensor has great potential in designing the working range and sensitivity by tailoring the porous structures.[40-42]

## Conflict of Interest

There is no conflict of interest.

## Supporting Information

Not applicable.

## References

[1] G. M. Sessler, J. Hillenbrand, Electromechanical response of cellular electret films, *Applied Physics Letters*, 1999, **75**, 3405-

3407, doi: 10.1063/1.125308.

[2] M. Lindner, H. Hoislbauer, R. Schwodiauer, S. Bauer-Gogonea, S. Bauer, Charged cellular polymers with "ferroelectretic" behavior, *IEEE Transactions on Dielectrics and Electrical Insulation*, 2004, **11**, 255-263, doi: 10.1109/tdei.2004.1285895.

[3] S. Bauer, R. Gerhard-Multhaupt, G. M. Sessler, Ferroelectrets: soft electroactive foams for transducers, *Physics Today*, 2004, **57**, 37-43, doi: 10.1063/1.1688068.

[4] M. Wegener, S. Bauer, Microstorms in cellular polymers: a route to soft piezoelectric transducer materials with engineered macroscopic dipoles, *ChemPhysChem*, 2005, **6**, 1014-1025, doi: 10.1002/cphc.200400517.

[5] D. Piazza, C. Galassi, A. Barzegar, D. Damjanovic, Dielectric and piezoelectric properties of PZT ceramics with anisotropic porosity, *Journal of Electroceramics*, 2010, **24**, 170-176, doi: 10.1007/s10832-008-9553-8.

[6] D. Zou, S. Liu, C. Zhang, Y. Hong, G. Zhang, Z. Yang, Flexible and translucent PZT films enhanced by the compositionally graded heterostructure for human body monitoring, *Nano Energy*, 2021, **85**, 105984, doi: 10.1016/j.nanoen.2021.105984.

[7] K.-I. Park, J. H. Son, G.-T. Hwang, C. K. Jeong, J. Ryu, M. Koo, I. Choi, S. H. Lee, M. Byun, Z. L. Wang, K. J. Lee, Highly-efficient, flexible piezoelectric PZT thin film nanogenerator on plastic substrates, *Advanced Materials*, 2014, **26**, 2514-2520, doi: 10.1002/adma.201305659.

[8] Y.-Y. Chiu, W.-Y. Lin, H.-Y. Wang, S.-B. Huang, M.-H. Wu, Development of a piezoelectric polyvinylidene fluoride (PVDF) polymer-based sensor patch for simultaneous heartbeat and respiration monitoring, *Sensors and Actuators A: Physical*, 2013, **189**, 328-334, doi: 10.1016/j.sna.2012.10.021.

[9] A. Mellinger, Dielectric resonance spectroscopy: a versatile tool in the quest for better piezoelectric polymers, *IEEE Transactions on Dielectrics and Electrical Insulation*, 2003, **10**, 842-861, doi: 10.1109/Tdei.2003.1237333.

[10] R. H. Ali Samadi, T. Azdast, H. Abdollahi, P. Zarrintaj, M. R. Saeb, Piezoelectric performance of microcellular polypropylene foams fabricated using foam injection molding as a potential scaffold for bone tissue engineering, *Journal of Macromolecular Science, Part B*, 2020, **59**, 14, doi: 10.1080/00222348.2020.1730573

[11] X. Zhang, L. Wu, G. M. Sessler, Energy harvesting from vibration with cross-linked polypropylene piezoelectrets, *AIP Advances*, 2015, **5**, 077185, doi: 10.1063/1.4928039.

[12] X. Zhang, J. Huang, J. Chen, Z. Wan, S. Wang, Z. Xia, Piezoelectric properties of irradiation-crosslinked polypropylene ferroelectrets, *Applied Physics Letters*, 2007, **91**, 182901, doi: 10.1063/1.2803316.

[13] M. Wegener, W. Wirges, J. Fohlmeister, B. Tiersch, R. Gerhard-Multhaupt, Two-step inflation of cellular polypropylene films: void-thickness increase and enhanced electromechanical properties, *Journal of Physics D: Applied Physics*, 2004, **37** 623, doi: 10.1088/0022-3727/37/4/013.

[14] Y. Li, C. Zeng, Low-temperature $CO_2$-assisted assembly of cyclic olefin copolymer ferroelectrets of high piezoelectricity and thermal stability, *Macromolecular Chemistry and Physics*, 2013, **214**, 2733-2738, doi: 10.1002/macp.201300440.

[15] H. Wang, Y. Li, X. Wang, Z. Liu, M. F. Ahmed, C. Zeng, Preparation and Characterization of Piezoelectric Foams Based on Cyclic Olefin Copolymer, *Engineered Science*, 2021, **16**, 203-210, doi: 10.30919/es8d560.

[16] Z. Liu, M. Zeng, H. Wang, X. Wang, Y. Li, C. Zeng, Toward Flexible Piezoelectrets with High Environmental Stability: A Hybrid Approach, *ES Materials & Manufacturing*, 2022, **17**, 73-82, doi: 10.30919/esmm5f631.

[17] R. Pisani Altafim, D. Rychkov, W. Wirges, R. Gerhard, H. Basso, R. Correa Altafim, M. Melzer, Laminated tubular-channel ferroelectret systems from low-density polyethylene films and from fluoroethylene- propylene copolymer films - A comparison, *IEEE Transactions on Dielectrics and Electrical Insulation*, 2012, **19**, 1116-1123, doi: 10.1109/tdei.2012.6259978.

[18] Altafim, Basso, Altafim, Lima, D. Aquino, Neto, Gerhard-Multhaupt, Piezoelectrets from thermo-formed bubble structures of fluoropolymer-electret films, *IEEE Transactions on Dielectrics and Electrical Insulation*, 2006, **13**, 979-985, doi: 10.1109/tdei.2006.247822.

[19] O. Voronina, M. Wegener, W. Wirges, R. Gerhard, L. Zirkel, H. Münstedt, Physical foaming of fluorinated ethylene-propylene (FEP) copolymers in supercritical carbon dioxide: single-film fluoropolymer piezoelectrets, *Applied Physics A*, 2008, **90**, 615-618, doi: 10.1007/s00339-007-4371-4.

[20] P. Fang, X. Qiu, W. Wirges, R. Gerhard, L. Zirkel, Polyethylene-naphthalate (PEN) ferroelectrets: cellular structure, piezoelectricity and thermal stability, *IEEE Transactions on Dielectrics and Electrical Insulation*, 2010, **17**, 1079-1087, doi: 10.1109/tdei.2010.5539678.

[21] K. Sappati, S. Bhadra, Piezoelectric polymer and paper substrates: a review, *Sensors*, 2018, **18**, 3605, doi: 10.3390/s18113605.

[22] R. Alberto Pisani Altafim, X. Qiu, W. Wirges, R. Gerhard, R. Alberto Corrêa Altafim, H. C. Basso, W. Jenninger, J. Wagner, Template-based fluoroethylenepropylene piezoelectrets with tubular channels for transducer applications, *Journal of Applied Physics*, 2009, **106**, 014106, doi: 10.1063/1.3159039.

[23] A. Savolainen, K. Kirjavainen, Electrothermomechanical film. part I. design and characteristics, *Journal of Macromolecular Science: Part A - Chemistry*, 1989, **26**, 583-591, doi: 10.1080/00222338908051994.

[24] M. K. Hämäläinen, J. K. Parviainen, T. Jaaskelainen, A novel micromovement actuator manufactured using plastic electromechanical film, *Review of Scientific Instruments*, 1996, **67**, 1598-1601, doi: 10.1063/1.1146867.

[25] P. Pondrom, J. Hillenbrand, G. M. Sessler, J. Bos, T. Melz, Energy harvesting with single-layer and stacked piezoelectret films, *IEEE Transactions on Dielectrics and Electrical Insulation*, 2015, **22**, 1470-1476, doi: 10.1109/tdei.2015.7116339.

[26] X. Zhang, G. M. Sessler, Y. Wang, Fluoroethylenepropylene ferroelectret films with cross-tunnel structure for piezoelectric transducers and micro energy harvesters, *Journal of Applied*

*Physics*, 2014, **116**, 074109, doi: 10.1063/1.4893367.

[27] G. M. Sessler, G. M. Yang, W. Hatke, Electrical Insulation and Dielectric Phenomena, IEEE 1997 Annual Report, 1997, **2**, 467-470, 10.1109/CEIDP.1997.641113

[28] L. J. Gibson, M. F. Ashby, Cellular Solids, Cambridge: Cambridge University Press, 1997, doi: 10.1017/cbo9781139878326.

[29] J. Hillenbrand, G. M. Sessler, Dielectrics and Electrical Insulation, *IEEE Transactions on Dielectrics and Electrical Insulation*, 2000, **7**, 537-542, doi; 10.1109/94.868074.

[30] K. Kim, W. Zhu, X. Qu, C. Aaronson, W. R. McCall, S. Chen, D. J. Sirbuly, 3D optical printing of piezoelectric nanoparticle-polymer composite materials, *ACS Nano*, 2014, **8**, 9799-9806, doi: 10.1021/nn503268f.

[31] F. Bos, R. Wolfs, Z. Ahmed, T. Salet, Additive manufacturing of concrete in construction: potentials and challenges of 3D concrete printing, *Virtual and Physical Prototyping*, 2016, **11**, 209-225, doi: 10.1080/17452759.2016.1209867.

[32] Y. Hwang, O. H. Paydar, R. N. Candler, 3D printed molds for non-planar PDMS microfluidic channels, *Sensors and Actuators A: Physical*, 2015, **226**, 137-142, doi: 10.1016/j.sna.2015.02.028.

[33] X. Wang, Z. Liu, H. Wang, C. Zeng, Direct 3D Printing of Piezoelectrets: Process Feasibility, Prototypes Fabrication and Device Performance, Engineered Science, *Engineered Science*, 2023, **21**, 800, doi: 10.30919/es8d800

[34] G. L. Goh, V. Dikshit, R. Koneru, Z. K. Peh, W. Lu, G. Dong Goh, W. Y. Yeong, Fabrication of design-optimized multifunctional safety cage with conformal circuits for drone using hybrid 3D printing technology, *The International Journal of Advanced Manufacturing Technology*, 2022, **120**, 2573-2586, doi: 10.1007/s00170-022-08831-y.

[35] A. Roshanghias, M. Krivec, M. Baumgart, Sintering strategies for inkjet printed metallic traces in 3D printed electronics, *Flexible and Printed Electronics*, 2017, **2**, 045002, doi: 10.1088/2058-8585/aa8ed8.

[36] E. Sowade, M. Polomoshnov, A. Willert, R. R. Baumann, Toward 3D-printed electronics: inkjet-printed vertical metal wire interconnects and screen-printed batteries, *Advanced Engineering Materials*, 2019, **21**, 1900568, doi: 10.1002/adem.201900568.

[37] W. S. Boyle, P. Kisliuk, Departure from Paschen's Law of Breakdown in Gases, *Physical Review*, 1955, **97**, 255-259, doi: 10.1103/PhysRev.97.255.

[38] E. Husain, R. S. Nema, Analysis of paschen curves for air, N2 and SF6 using the townsend breakdown equation, *IEEE Transactions on Electrical Insulation*, 1982, **EI-17**, 350-353, doi: 10.1109/tei.1982.298506.

[39] H. Nahvi, M. Jabbari, Crack detection in beams using experimental modal data and finite element model, *International Journal of Mechanical Sciences*, 2005, **47**, 1477-1497, doi: 10.1016/j.ijmecsci.2005.06.008.

[40] A. K. Sinha, G. L. Goh, W. Y. Yeong, Y. Cai, Ultra-low-cost, crosstalk-free, fast-responding, wide-sensing-range tactile fingertip sensor for smart gloves, *Advanced Materials Interfaces*, 2022, **9**, 2200621, doi: 10.1002/admi.202200621.[LinkOut]

[41] M. F. Mabrook, C. Pearson, A. S. Jombert, D. A. Zeze, M. C. Petty, The morphology, electrical conductivity and vapour sensing ability of inkjet-printed thin films of single-wall carbon nanotubes, *Carbon*, 2009, **47**, 752-757, doi: 10.1016/j.carbon.2008.11.009.

[42] Z. Guo, P. Yu, Y. Liu, J. Zhao, Pre-fatigue enhancing both long-term stability and sensitivity of direct-ink-writing printed sensors, *International Journal of Fatigue*, 2023, **166**, 107237, doi: 10.1016/j.ijfatigue.2022.107237.